crystals

MDPI

Article

Automated and Selective Product Removal for Lab-Scale Draft Tube Baffle Crystallizer Under Vacuum Operation

Laura Marsollek, Merlin Hubmann, Kim Buchhorn and Norbert Kockmann *

Laboratory of Equipment Design, Department of Chemical and Biochemical Engineering, TU Dortmund University, Emil-Figge-Str. 68, 44227 Dortmund, Germany; laura.marsollek@tu-dortmund.de (L.M.)
* Correspondence: norbert.kockmann@tu-dortmund.de

Abstract

Continuous product removal in lab-scale vacuum applications poses significant challenges, particularly due to the risk of clogging in the product tube caused by the small tubing diameter relative to the particle size. This contribution addresses this problem by presenting an automatic gate system specifically designed for selective product removal within a Draft Tube Baffle Crystallizer (DTBC). In order to enable selective product removal, the classification behavior of the crystals in the DTBC was evaluated in experimental studies by determining the crystal size distributions in the product removal and in the fine grain dissolution. The influence of different stirring speeds and solid contents were considered for different product removal rates. The results indicated that sufficient classification occurs at stirring speeds of 600 rpm and a crystal content of $\geq$3 wt%. Under these conditions, more than 75% of the crystals in the product were larger than 210 µm from a sieve size range of 45 to 500 µm. During experiments, the automatic gate system allowed for blockage-free, continuous product removal for six hours per experiment and more than thirty hours in total, proving the reliability of the system. Although designed for down-scaling of the DTBC, this system can also be applied to other continuous-flow lab-scale applications.

Keywords: automation; DTBC; lab-scale crystallization; product removal; vacuum crystallization

check for updates

Academic Editor: Jean-Marc Haudin

Received: 29 August 2025
Revised: 8 October 2025
Accepted: 12 October 2025
Published: 15 October 2025

Citation: Marsollek, L.; Hubmann, M.; Buchhorn, K.; Kockmann, N. Automated and Selective Product Removal for Lab-Scale Draft Tube Baffle Crystallizer Under Vacuum Operation. *Crystals* **2025**, *15*, 893. https://doi.org/10.3390/cryst15100893

Copyright: © 2025 by the authors. Licensee MDPI, Basel, Switzerland. This article is an open access article distributed under the terms and conditions of the Creative Commons Attribution (CC BY) license (https://creativecommons.org/licenses/by/4.0/).

1. Introduction

The paradigm shift from batch to continuous crystallization equipment marks a significant advancement in small-scale production and process development, particularly within the pharmaceutical and specialty chemistry industries [1–8]. This transition is driven by the need for increased flexibility and efficiency, allowing for rapid adjustments to market demands [9–11].

Crystallization is a separation and purification process that is widely used in the process industry [12,13]. For many industrial crystallization processes, a draft tube baffle crystallizer (DTBC) is utilized. The most common application of this type of crystallizer is as an evaporative crystallizer for substances whose solubility depends only slightly on temperature [14–17]. However, it is also employed for antisolvent [18] or cooling crystallization [19]. Among various crystallizer types, the DTBC is prominent for its characteristic hydrodynamic behavior, which enables effective particle separation in the DTBC and thus a narrow crystal size distribution (CSD) in the product [15,17,20]. To create this hydrodynamic behavior, a stirrer at the bottom of the DTBC generates a circulation flow by conveying the suspension from the body of the DTBC through the tube upward

into the head, where it then flows back down between the tube and the outer wall in the annular gap. Due to the discontinuous cross-sectional jump as it flows back into the DTBC body, a classifier zone is formed that enables particle separation. Within the classifier zone, the particles separate based on their specific settling velocity, with smaller particles being drawn into the fine grain dissolution (FGD) for complete dissolution, while larger particles settle down with the gravitational force [21]. While the DTBC in an industrial scale has been investigated in many aspects such as the hydrodynamic behavior with Computational Fluid Dynamics (CFD) simulations [22–26], the influence of the dissolution of fine grain in the FGD [27–29] and scale-up studies [30,31], the research on lab-scale DTBC has been limited on the startup behavior and residence time distribution during cooling crystallization [19,32]. The implementation of evaporation crystallization in a lab-scale DTBC is hampered by the FGD functionality. Further heating of the suspension in the FGD through the heat exchanger can cause unwanted evaporation of the solution in the FGD, potentially leading to uncontrolled crystallization. Adding geodetic height to the FGD increases the local pressure in the FGD and, consequently, the boiling point. This prevents evaporation in the FGD and creates a small operating window for the dissolution of fine grain in the FGD in a lab-scale DTBC [33]. However, during continuous cooling crystallization blockages occurred [19], particularly affecting the product removal due to high crystal content. Therefore, a reliable product removal system is important, ensuring that crystals are extracted without dead zones and with minimal stress to avoid mechanical strain and abrasion that could compromise quality [34]. Since the DTBC is also used for vacuum evaporation crystallization, the product removal must be vacuum-tight as well.

Peristaltic pumps are typically used for the continuous conveying of crystallization suspensions due to their affordability and adjustable flow rate [35]. However, this approach is not suitable for lab-scale vacuum applications, since collapsing prevents the use of sufficiently large tubing inner diameters to avoid clogging in the product tube. Gravimetric transfer via an overflow tube does not affect crystal size, but it requires a relatively homogeneous suspension in the crystallizer, making it particularly suitable for stirred tank and ideally mixed crystallizers [36]. Schmalenberg et al. [32] introduced a novel particle screw for efficient product removal, showing promising results for cooling crystallization. However, vacuum tightness is only achievable with a peristaltic pump, limiting its use under vacuum conditions.

For the enhancement of crystallization process performance, larger crystals can be selectively removed from the product. By using a so-called external classification, a partial stream is drawn from the crystallizer and large product crystals are separated using a hydrocyclone. In this method, part of the feed stream is fed through an inlet pipe positioned centrally at the bottom of the DTBC. In this pipe, only large crystals sediment against the upward flow generated in this way and are discharged at the bottom of the pipe [26,37]. However, these approaches are not applicable on a laboratory scale. The required upward flows are too high to be achieved by the feed flow, due to the small diameter. An alternative approach is the adjustment of the process parameters to influence the hydrodynamic behavior in such a way that large crystals with a narrow particle size distribution are preferentially discharged [24,25,38–41].

In this study a gate system for product removal from a DTBC with minimal impact on the crystallization process is presented. Similar to Acevedo et al. [42], a transfer zone is created between two valves where the suspension flows in by gravity when the upper valve is opened. By evacuating the transfer zone, the influence on vacuum evaporation during crystallization can be minimized. The fully automated product removal system allows for semi-continuous product removal with a defined product removal rate through adjustable opening intervals.

The objective of this work is to investigate the influence of the volume flow in the FGD, the product removal rate, the stirring speed, and the solid content in suspension on the sedimentation behavior in a DTBC using the developed gate system. Therefore, the process parameters are systematically changed and the CSD in the FGD, and in the product, are examined. The aim is to enable process optimization through a selective product removal, which will ensure a narrow CSD on the product and compliance with the operating window of the FGD for evaporation crystallization. In addition, a reliable approach for continuous product removal in lab-scale application is demonstrated through the developed gate system, with its design and automation detailed in this work.

2. Materials and Methods

The classification experiments are conducted in a lab-scale DTBC made out of glass (glassblower workshop, TU Dortmund University, Dortmund, Germany) with an inner volume of 2.1 L. As test system, a binary model system of deionized water (<10 µS cm^{-1}) and the amino acid L-alanine was used. The density difference between L-alanine and water at 45.8 °C is 375 kg m^{-3} [43] and the experimentally determined correlation of solubility according to Wohlgemuth and Schembecker [44] was applied to determine the solubility. Further properties of the test system can be found in the Supporting Information (SI), Section S1. The experiments were carried out at a temperature of 45.9 °C.

2.1. Experimental Setup

This study investigates the classification within a DTBC by analyzing the CSD at various locations. A defined CSD is added to the solution instead of being grown in the DTBC, allowing the impact of hydrodynamic behavior to be assessed independently.

The characteristic vertical flow in the DTBC is generated by a five-blade diagonal stirrer made of glass (glassblower workshop, TU Dortmund, Dortmund, Germany) with a diameter of 35 mm and a height of 20 mm. The stirrer blade is positioned directly at the end of the DT over the W-shaped bottom and is driven by a laboratory motor RZR 2102 Control from Heidolph Scientific Products GmbH (Schwabach, Germany). The heat is supplied to the suspension in the DTBC by a two-stage heating jacket, which is circulated with deionized water from a thermostat (Thermostat 01, Pilot One Ministat 125, Huber Kältemaschinen GmbH, Offenburg, Germany). The inlet into the FGD is located on the upper right side of the DTBC body and the volume flow rate in the FGD ($\dot{V}_{FGD}$) is adjusted using a Watson peristaltic pump (120S/DV, Watson-Marlow Pumps Group, Wilmington, DE, USA). A sampling point for the FGD is placed behind the pump. The polyvinyl chloride tubes of the FGD with an inner diameter of 3.2 mm (Tygon®, Saint-Gobain Corporation, Malvern, PA, USA) were insulated with a tube heater due to the temperature dependence of the L-alanine solubility in water. The water temperature in the tube heater was maintained at 45 °C using a thermostat (Ministat 230, Huber Kältemaschinen GmbH, Offenburg, Germany). In order to avoid any impacts on the added CSD, no heat exchanger is implemented in the FGD.

The product removal is positioned at the bottom of the DTBC, opposite the FGD. In order to ensure that the least amount of product is withdrawn and to maintain a constant CSD during the tests, the volume flow of the product ($\dot{V}_{Prod}$) is recirculated back into the DTBC. For this purpose, a heated, double-walled glass vessel is used to collect the product and the suspension is pumped back into the head of the DTBC by a peristaltic pump (LabDos easy-load, HiTec Zang GmbH, Herzogenrath, Germany) with a volume flow of 200 mL min^{-1}. To prevent blockages, a tube with an inner diameter of 6.35 mm (TY6,35AG9,53, Norprene® A-60-G, Saint-Gobain Performance Plastics Corporation, La Défense Cedex, France) is used. The entire setup is shown schematically in Figure 1. A

list of all equipment used can be found in the SI, Table S1 and detailed information to the geometry of the DTBC is given in Figure S1.

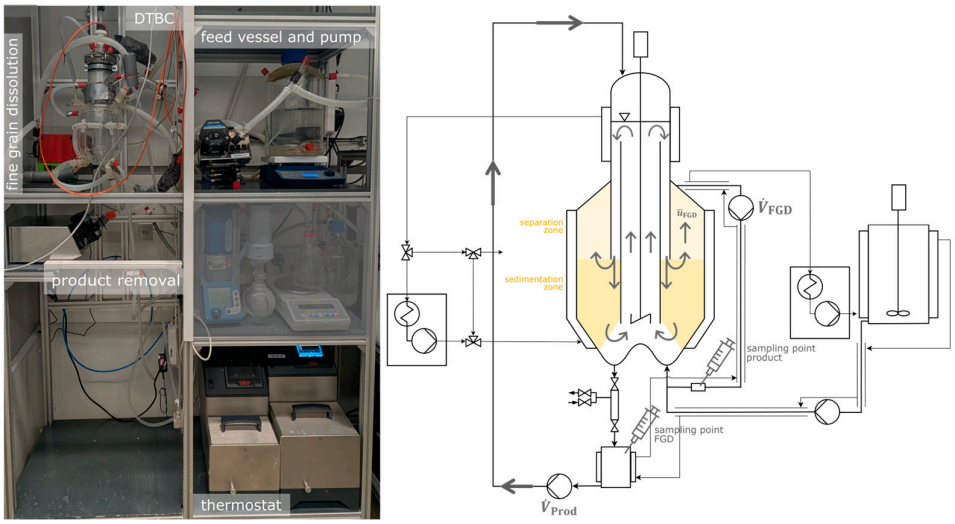


Figure 1. Experimental setup used for the classification experiments (**left**) and the corresponding flow scheme showing the flow pattern, with the flow direction is indicated by arrows (**right**).

2.2. Product Removal System

A reliable product removal system is crucial for the realization of continuous crystallization. However, only a few solutions are available, especially for vacuum applications in a laboratory scale. For this reason, a product removal system has been developed that is suitable for removing solid products from laboratory equipment under vacuum, in particular from a lab-scale DTBC. The developed product removal system is based on the concept of a gate system, in which a gate volume is created between two valves that are opened and closed sequentially. By opening the upper valve, the suspension enters the previously evacuated gate volume. This minimizes the influence of product removal on the vacuum inside the DTBC. After the upper valve is closed, the gate volume is opened to ambient pressure so that the product suspension can be drained by opening the lower valve. In addition, the gate volume can be pressurized with 2 bar compressed air to flush out any remaining suspension from the gate volume. A flow sheet of the automated gate system is shown in Figure 2.

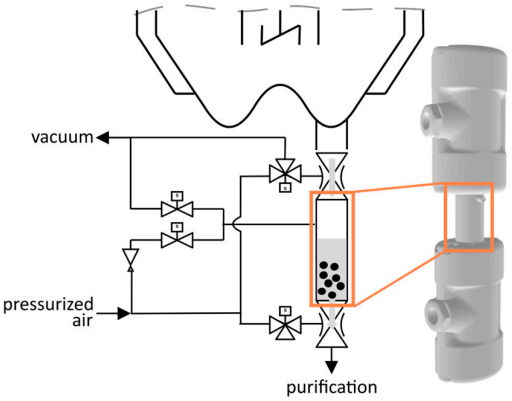


Figure 2. Flow scheme of the automated gate system and the pressurized air control circuit with black dots representing the crystals.

Two pinch valves with an inner diameter of 10 mm (VMP010.03XK.72, AKO Armaturen & Separationstechnik GmbH, Trebur, Germany) are used for the gate system, as the

inner diameter is only minimally reduced and no dead spaces occur. Due to the pneumatic control, a short setting time of approx. 0.05 s is achieved, enabling a defined product removal per valve opening. By quickly repeating the valve openings, an almost continuous product removal is possible. The pressurized air supply for opening the pinch valves is controlled by two 3/2-way solenoid valves (M07310HN/24DC, AKO Armaturen & Separationstechnik GmbH, Trebur, Germany). Further information about the developed gate system and the automation and the calibration is given in the SI, Figures S4–S7 and Section S3.

Although the product removal system was specifically designed for application in a DTBC, it is equally suitable for other lab-scale operations under vacuum. The connection via DIN G3/8 fittings (Bohlender GmbH, Grünsfeld, Germany) enables straightforward integration with standard process equipment. The product removal rate is limited only by the valve switching time of approximately 0.05 s and the time required for evacuation of the gate volume. The calibration of the pinch valves with respect to the opening time of the upper valve is provided in the SI, Figure S6. Furthermore, the automation concept is readily adaptable, as the control function is simple and can be implemented in other programming languages as well.

2.3. Experimental Procedure

For characterizing the classification in lab-scale DTBC, a suspension with a defined CSD is used. Therefore, six crystal classes were defined and added to the solution in equal weight proportions: 0–45 µm, 45–90 µm, 90–180 µm, 180–250 µm, 250–355 µm, and 355–500 µm.

The crystals are prepared through grinding and sieving and three samples are taken to determine the initial CSD (CSD_{init}). The saturated solution is prepared at least 12 h before the experiments at 55 °C in a feed vessel and subsequently pumped into the DTBC before the experiments. Before setting the desired stirring speed, the crystals are seeded into the saturated solution within the DTBC. The flow rate of $\dot{V}_{FGD}$ is set by the peristaltic pump in the FGD, while the flow rate for $\dot{V}_{Prod}$ is set through the opening intervals of the gate system.

The operating ranges for $\dot{V}_{Prod}$ and $\dot{V}_{FGD}$ are defined using the fines-removal rate R in Equation (1) [13]. The fines removal rate relates the dissolution of the fine grain to the product removal rate, providing a measure to define a stable crystallization process, typically within the range of 2.62 to 6.55 [29,45].

$$R = \frac{\dot{V}_{FGD} + \dot{V}_{Prod}}{\dot{V}_{FGD}} \quad (1)$$

Due to the potential evaporation of the solution in the FGD, only a narrow operating window with a limited temperature range is feasible. Preliminary experiments were conducted to determine the maximum $\dot{V}_{FGD}$, at which complete dissolution were achieved for fine particles with a crystal size of 90 µm and a solid content of 0.5 wt%. Therefore, 25 mL min^{-1} ± 5 mL min^{-1} is chosen as the operating range for $\dot{V}_{FGD}$. By applying the recommended R = 2.76 for a stable evaporation crystallization proposed by Sutradhar and Randolph [27], an operating point for $\dot{V}_{Prod}$ of 15 mL min^{-1} was calculated. For defining an operating range for $\dot{V}_{Prod}$, the operating points at $\dot{V}_{Prod}$ ± 5 mL min^{-1} were also examined. Prior to the classification experiments, it was experimentally determined that complete suspension of the crystals in the lab-scale DTBC is achieved at a stirring speed of 800 rpm. To enable sedimentation of the product crystals, stirring speeds of 500, 600, and 700 rpm were investigated. The impact of $\dot{V}_{Prod}$, $\dot{V}_{FGD}$, and stirring speed on classification

is examined by considering all parameter combinations, resulting in a total of 27 operating points. The investigated parameters are summarized in Table 1.

Table 1. Experimental schedule with all operating points for the stirring speeds 500, 600, and 700 rpm at 1 wt%.

Operating Point	$\dot{V}_{Prod}$ [mL min^{-1}]	$\dot{V}_{FGD}$ [mL min^{-1}]
OP1–OP3	10	20, 25, 30
OP4–OP6	15	20, 25, 30
OP7–OP9	20	20, 25, 30

The experiments are carried out at a constant solid content of 1 wt% and a constant stirring speed, whereas a variation of $\dot{V}_{Prod}$ and $\dot{V}_{FGD}$ led to a total of nine operating points per experiment. In order to investigate the classification for different points in time during the crystallization process, experiments are carried out at higher solid contents of 3 wt% and 5 wt% at a $\dot{V}_{Prod}$ = 20 mL min^{-1} and $\dot{V}_{FGD}$ = 30 mL min^{-1}. All experiments are conducted three times.

2.4. Image Analysis and Determination of the CSD

The classification within the DTBC is evaluated based on the CSD in the product (CSD_{Prod}) and the FGD (CSD_{FGD}). For this purpose, two samples are taken with a preheated syringe for each operating point: one from the sampling point of the FGD and the other from the product vessel. To counteract potential changes in crystal size, crystals are directly separated from the saturated solution by filtration, dried, and resuspended in 5 mL of ethanol, in which L-alanine has low solubility. The workflow for sample preparation was adapted from the method described by Höving et al. [46] and is illustrated in Figure S2. The crystals in the resuspended samples are photographed in a Petri dish at 10× magnification (DIN lens 10×, Bresser GmbH, Rhede, Germany) using a Nikon Z6 II camera (Nikon Corporation, Tokyo, Japan), as shown in Figure S3 in the SI. To ensure that no crystal is photographed twice, squares of cm^2 are defined using graph paper, which are subsequently focused on in the photographs.

For a representative CSD, the crystal size of at least 200 crystals per operating point are determined. The Feret diameter was determined according to [47]. In Figure 3, the marking of the crystals with polygons and ovals for determining the Feret diameter is exemplarily illustrated.

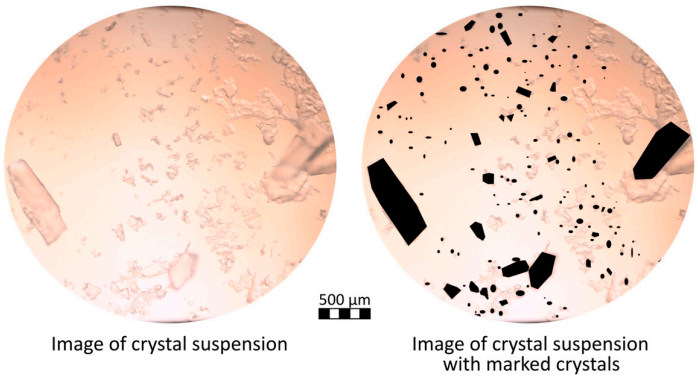


Figure 3. Exemplary representation of marked crystals for determining the Feret diameter.

From the total number of particle sizes determined according to the Feret diameter, the CSD was calculated according to Equation (2) and density distribution $q_{r,i}$ according to

Equation (3). For r = 0, 1, or 2, the distribution is characterized either by the number, length, or area of the crystals.

$$Q_{r,i} = Q_r(x_i) = \frac{x_{100} - x_i}{x_{100}} \tag{2}$$

$$q_{r,i} = \frac{x_{100} - x_\mathrm{i}}{x_{100}\ \Delta x_i} \tag{3}$$

The relative frequency $q_{r,i}$ is calculated by normalizing $Q_{r,i}$ over the interval width Δx_i. The variable x_i defines a crystal size threshold for a certain percentage i, which describes percentiles at different levels with a range of i = 1, 2, …, n. Accordingly, x_{100} represents the maximum crystal size below which 100% of the crystal population is contained. For an intuitive understanding, the CSD are evaluated based on the resulting Q_0 distributions. Additionally, the distributions are visualized using boxplots, which allow estimation of statistical values such as median (x_{50}). The central crystal size in the distribution is characterized by x_{50}, indicating the crystal size above which 50% of the crystals are larger. The 25th and 75th percentiles (x_{25} and x_{75}) define lower and upper edges of the boxplots, corresponding to the particle sizes below which 25% and 75% of the crystals fall, respectively. To assess the homogeneity of the particle size distribution, the interquartile range (IQR) as a difference between x_{25} and x_{75} is calculated. Since the focus of this work is on the quantitative comparison of the distributions rather than on exact statistical values, the percentiles are approximated from the boxplots [12,48,49].

2.5. Description of the Suspension Behavior

The classification in the DTBC depends mainly on particle separation in the separation zone in the upper half of the DTBC body (see Figure 1). Within this zone, the particle separation is influenced by gravity, the flow regime, and the inflow velocity into the FGD $\overline{u}_\mathrm{FGD}$. To describe particle separation, $\overline{u}_\mathrm{FGD}$ is calculated using Equation (4), while the specific particle settling velocity w_s is described by Equation (5), assuming perfectly spherical particles [50].

$$\overline{u}_\mathrm{FGD} = \frac{\dot{V}_\mathrm{FGD}}{\frac{\pi}{4}\, d_\mathrm{FGD}^2} \tag{4}$$

$$w_\mathrm{s} = \sqrt{\frac{4}{3}\,\frac{(\rho_\mathrm{S} - \rho_\mathrm{L})\, g\, x_\mathrm{p}}{\rho_\mathrm{L}\, c_\mathrm{w}(Re)}} \tag{5}$$

Since the diameter of the FGD inlet connector (d_FGD) cannot be modified during the experiments, any change of $\overline{u}_\mathrm{FGD}$ can only be achieved by adjusting $\dot{V}_\mathrm{FGD}$, according to Equation (4). In addition to the crystal density ρ_S and the solution density ρ_L, the settling velocity w_s depends on gravity g and the particle size x_p. Furthermore, w_s is influenced by the drag coefficient $c_\mathrm{w}(Re)$, which is a function of the Reynolds number and thus of the prevailing flow regime. For crystal separation, the criterion $w_\mathrm{s} < \overline{u}_\mathrm{FGD}$ must be fulfilled. The crystal size at which both velocities are equal is referred to as the cut-off particle size. Crystals larger than this threshold remain in the DTBC and settle down in the sedimentation zone in the lower half of the DTBC body, whereas smaller ones are withdrawn into the FGD and dissolved.

In the sedimentation zone, interactions between particles lead to a kind of collective hindrance effect, in which the upward flow of fluid between the settling particles slows down the sinking of the neighboring particles. To account for the influence of the volume fraction of particles in the suspension on the cut-off particle size, the approach of Richardson-Zaki in Equation (6) is used to calculate the swarm settling velocity w_ss.

This approach considers the particle volume fraction φ and the flow regime through the exponent n.

$$w_{ss} = w_s \, (1 - \varphi)^n \tag{6}$$

According to Equation (6), particles in suspensions with high solid concentrations exhibit lower settling velocities than those in dilute suspensions [49]. The energy introduced by stirring counteracts the sedimentation of the particles. Due to its influence on the flow regime, the stirring speed has a direct effect on w_s and thus on the cut-off particle size.

3. Results and Discussion

The presented setup and methodology are designed to investigate the characteristic classification of crystals along the DTBC body. The objective is to characterize how changes in process parameters affect the hydrodynamic behavior within the DTBC and the suspension behavior of the crystals. This allows assessment of how the CSD in the product and the FGD can be influenced by targeted adjustment of $\dot{V}_{\mathrm{Prod}}$ and $\dot{V}_{\mathrm{FGD}}$, and the stirring speed for different solid contents in the suspension. The experiments are based on the added $\mathrm{CSD_{init}}$, which contains equal weight proportions of six crystal size classes. To evaluate classification, $\mathrm{CSD_{FGD}}$ and $\mathrm{CSD_{Prod}}$ are compared to $\mathrm{CSD_{init}}$. The relative frequency q_0 and the cumulative distribution Q_0 of $\mathrm{CSD_{init}}$ are shown in Figure 4.

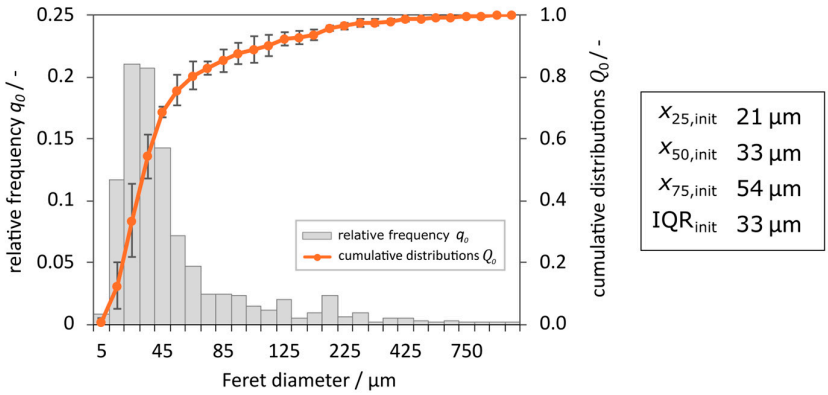


Figure 4. The relative frequency q_0 and cumulative distribution Q_0 of $\mathrm{CSD_{init}}$ with the statistical values.

As shown by the relative frequency q_0 in Figure 4, the peak, and thus the majority of particles, occurs at approximately 30 µm. Around this value the particle distribution is narrow. For particle sizes above 30 µm, the distribution decreases sharply with increasing crystal size, so that only scattered particles were counted for crystal sizes > 500 µm. This is also apparent in the cumulative distribution function, which shows a steep rise at the beginning and then flattens out, indicating that the initial distribution contains many smaller crystals with a size above 100 µm but few larger ones. These observations are confirmed by the statistical values. The median value of $\mathrm{CSD_{init}}$ is $x_{50,\mathrm{init}}$ = 33 µm, while $x_{25,\mathrm{init}}$ = 21 µm, indicating the narrow distribution of small particles characterized by an $\mathrm{IQR_{init}}$ of 33 µm. Furthermore, a strong decrease in the relative frequency q_0 for particles larger than 50 µm is observed, which is also evident by a value of $x_{50,\mathrm{init}}$ = 54 µm.

Since a higher number of smaller particles is required to achieve the same weight as larger crystals, the shift towards smaller particles in $\mathrm{CSD_{init}}$ can be explained by using equal masses of each crystal class. Maintaining a clear classification effect in the product requires minimizing the sedimentation of smaller crystals into the product stream to achieve a high $x_{25,\mathrm{Prod}}$. For the $\mathrm{CSD_{FGD}}$, a clear classification is not expected, since the initial distribution is already close to the expected $\mathrm{CSD_{FGD}}$ with $x_{75,\mathrm{FGD}}$ < 100 µm. Instead, the focus is

on minimizing the number of large crystals entering the FGD, keeping $x_{75,FGD}$ as low as possible.

3.1. Impact of Different Flow Rates

The particle separation and classification in the DTBC is based on the particle velocity in the separation zone. As described in Section 2.5, the flow rate of $\dot{V}_{FGD}$ has a direct impact on the cut-off particle size, thereby influencing the classification within the DTBC. To characterize the actual influence of the flow rates of $\dot{V}_{FGD}$ and $\dot{V}_{Prod}$ on the classification, CSD_{Prod} and CSD_{FGD} will be examined at a solid content of 1 wt% and a stirrer speed of 500 rpm. Additionally, to account for potential correlations between the volume flow rates, every possible combination of $\dot{V}_{Prod}$ and $\dot{V}_{FGD}$ was considered. The corresponding boxplots of the resulting CSD_{FGD} are shown in Figure 5.

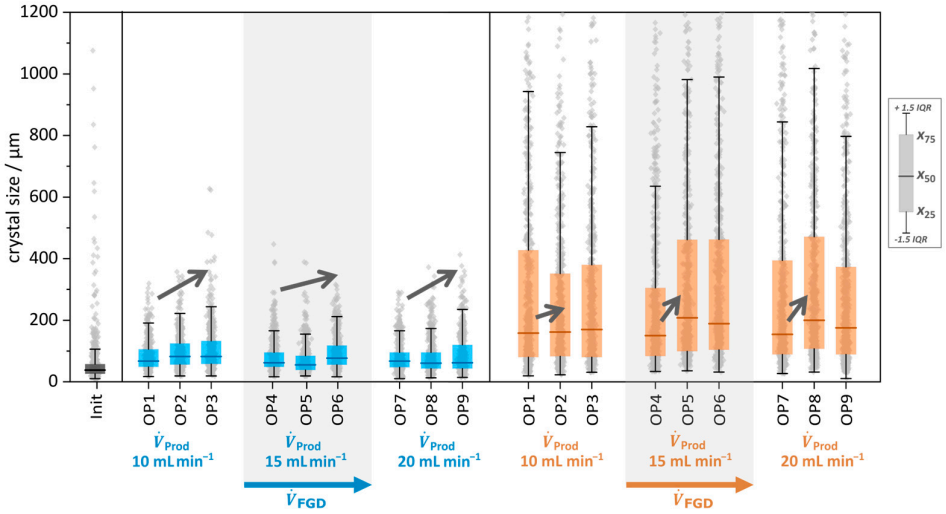


Figure 5. Boxplots comparing CSD_{FGD} (**blue**) and CSD_{Prod} (**orange**) for different flow rates of $\dot{V}_{Prod}$ and $\dot{V}_{FGD}$ at 500 rpm and a solid fraction of 1 wt% with CSD_{init} (**grey**). Arrows indicate the trend for increasing $\dot{V}_{FGD}$.

Figure 5 shows the boxplots of CSD_{FGD} and CSD_{Prod} in three blocks with constant $\dot{V}_{Prod}$ per block, in which $\dot{V}_{FGD}$ increases from left to right. The IQR and median values for CSD_{FGD} ($x_{50,FGD}$) and CSD_{Prod} ($x_{50,Prod}$) are higher than those for CSD_{init} for all operating points. For $\dot{V}_{Prod}$ = 10 mL min^{-1} and $\dot{V}_{FGD}$ = 20 mL min^{-1}, the highest values of approximately $x_{25,FGD}$ = 70 µm, $x_{50,FGD}$ = 90 µm, and $x_{75,FGD}$ = 130 µm are reached. Additionally, the whiskers and outliers of the boxplots show that crystals with a crystal size > 400 µm were counted in CSD_{FGD}. From this, it can be concluded that there is no sharp separation in the cut-off particle size, or that the cut-off particle size must be >400 µm.

For CSD_{Prod}, the expected classification effect of an DTBC is recognizable in the significant increase in statistical values across all operation points compared to CSD_{init}. The values of $x_{25,Prod}$ are above 100 µm and thus significantly above all values of $x_{75,init}$. The values of $x_{50,Prod}$ are above 170 µm and for $x_{75,Prod}$ at least above 300 µm.

A direct comparison of the statistical values for the different flow rates of $\dot{V}_{Prod}$ at the respective flow rate of $\dot{V}_{FGD}$ only shows a small increasing of the values of $x_{25,FGD}$, $x_{50,FGD}$, and $x_{75,FGD}$. When the influence of different $\dot{V}_{Prod}$ on CSD_{Prod} is compared, it becomes evident that the values of $x_{75,Prod}$ and $x_{50,Prod}$ for $\dot{V}_{Prod}$ = 15 and 20 mL min^{-1} are only slightly higher than for $\dot{V}_{Prod}$ = 10 mL min^{-1}. Therefore, the influence of $\dot{V}_{Prod}$ on the suspension behavior was considered to be minor.

However, when comparing the CSD_{FGD} for different $\dot{V}_{FGD}$ values, a particular increase in $x_{75,FGD}$ and IQR_{FGD} is observed with increasing $\dot{V}_{FGD}$. The highest statistical values are

consistently achieved at the maximum flow rate of $\dot{V}_{FGD}$ = 30 mL min^{-1}. The influence of $\dot{V}_{FGD}$ on CSD_{Prod} is evident from the increase in $x_{25,Prod}$ with increasing $\dot{V}_{FGD}$. Similar to the observations for CSD_{FGD}, the enhanced classification at higher $\dot{V}_{FGD}$ can be explained by an increasing $\overline{u}_{FGD}$, and consequently, a larger cut-off particle size, as described in Section 2.5. As a higher $\overline{u}_{FGD}$ leads to a higher likelihood of smaller crystals being entrained into the FGD instead of settling into the product removal, a higher product quality with higher flow rates of $\dot{V}_{FGD}$ were expected.

3.2. Impact of Different Stirring Speeds

The characteristic hydrodynamic behavior in the DTBC requires energy input from a stirrer. While ensuring circulation through the tube, the stirrer simultaneously generates turbulence in the crystallizer body, which counteracts sedimentation. To evaluate the influence of stirring speed on CSD_{Prod} and CSD_{FGD}, and to assess whether the effects observed for varying flow rates are also applicable at different stirring speeds, experiments were conducted at several rpm values for $\dot{V}_{FGD}$ = 30 mL min^{-1}. Since increasing the stirring speed affects the sedimentation behavior in the opposite way to the flow rate in the product removal, the CSDs are analyzed for different flow rates of $\dot{V}_{Prod}$ in Figure 6.

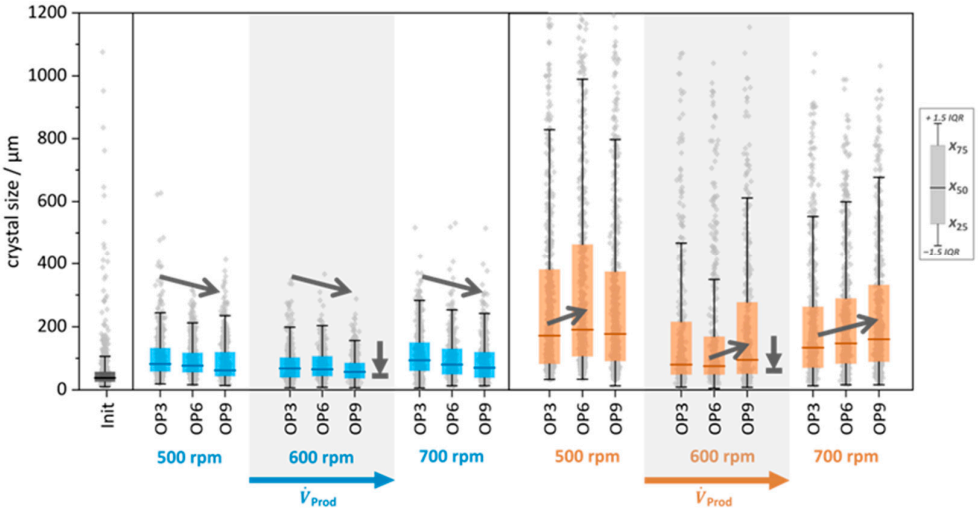


Figure 6. Boxplots comparing CSD_{FGD} (**blue**) and CSD_{Prod} (**orange**) for different stirring speeds and flow rates of $\dot{V}_{Prod}$ at $\dot{V}_{FGD}$ = 30 mL min^{-1} and at a solid fraction of 1 wt% with CSD_{init} (**grey**). Arrows indicate the trend for increasing $\dot{V}_{Prod}$ and highlight the lowest statistical values for x_{FGD} and x_{Prod}.

In Figure 6, the higher distributions of CSD_{FGD} and CSD_{Prod} compared to CSD_{init} indicates that a classification effect also occurs at higher stirrer speeds. Regardless of the stirring speed, it is observable, that an increase in $\dot{V}_{Prod}$ is associated with a decrease in the statistical values within the CSD_{FGD}. This suggests that fewer larger particles are being drawn into the FGD. Additionally, an increase of $x_{50,Prod}$ and $x_{25,Prod}$ is evident for higher flow rates in $\dot{V}_{Prod}$ in the CSD_{Prod}. Since $\dot{V}_{FGD}$ remains unchanged, this effect cannot be attributed to an increase in $\overline{u}_{FGD}$ but must instead result from the increase in w_s. A possible explanation for this observation is that opening the valve causes a sudden increase in the fluid velocity in the DTBC, which accelerates the settling of the particles in the sedimentation zone. Since smaller particles have already been separated in the separation zone and drawn into the FDG, they are less affected by the acceleration, which explains the decrease in $x_{50,FGD}$ and $x_{75,FGD}$. The diameter of the DTBC is ten-times larger than that of the product outlet, hence, according to mass conservation, this results in only a slight

increase in fluid velocity. Nevertheless, this acceleration may be sufficient at $\dot{V}_{Prod}$ = 15 and 20 mL min^{-1} to increase w_s and thereby enhance sedimentation.

By comparing the influence of the stirring speed on the classification, it can be seen, that for a stirring speed of 700 rpm, the values of $x_{50,Prod}$ are between 150–170 µm and $x_{75,Prod}$ between 250–350 µm, which is significantly lower than the values at a stirring speed of 500 rpm, where $x_{50,Prod}$ is between 180–200 µm and $x_{75,Prod}$ are between 380–440 µm. However, the most pronounced decrease in statistical values is observed at 600 rpm. For this stirring speed, the values of $x_{50,Prod}$ are between 100–120 µm and for $x_{75,Prod}$ between 170–240 µm. One possible explanation for the decrease in CSD_{Prod} at higher stirring speeds is a change in the height of the zones within the DTBC.

Figure S8 in the SI provides images of the separation and sedimentation zones at 600 rpm and 700 rpm. The separation zone can be identified as the region with less pronounced turbidity, which is attributable to a lower suspension density in this zone. As shown in Figure S8, with increasing rpm, the separation zone becomes progressively smaller, resulting in a lower suspension density in the sedimentation zone. According to Sha et al. [38], suspension density significantly influences classification, because w_{ss} decreases when the solid content is higher. This explains the improved classification observed at 700 rpm compared to 600 rpm. In contrast to 700 rpm, suspension density at 600 rpm is highest at the center of the DTBC, which most strongly restricts sedimentation in this region. At 500 rpm, the lower energy input from the stirrer is expected to result in an increased suspension density in the lower half of the DTBC, which means that particle separation in the classifier is less affected and large particles settle. Due to the enabled sedimentation, a higher proportion of larger particles is discharged during product removal.

3.3. Impact of Different Solid Fractions

In a continuous crystallization process, varying solid contents in the suspension are achieved depending on flow rates, energy input, and residence time. The particle settling velocity and the suspension behavior are influenced by these solid content variations. To investigate the impact of solid content on classification, CSD_{FGD} and CSD_{Prod} at solid contents of 1 wt%, 3 wt%, and 5 wt% are compared in Figure 7. Similar to the analysis of stirring speed effects, the experiments are conducted at flow rates of $\dot{V}_{FGD}$ = 30 mL min^{-1} and $\dot{V}_{Prod}$= 20 mL min^{-1}. To ensure sufficient suspension even at higher solid contents, the experiments are performed at stirring speeds of 600, 700, and 800 rpm.

For the influence of the stirring speed on CSD_{FGD} at higher solid fractions, Figure 7 shows an increase in $x_{50,FGD}$, $x_{25,FGD}$, $x_{75,FGD}$, and IQR_{FGD}. This observation is consistent with the results for increased stirring speed at a solid content of 1 wt%, where the statistical values also increased with higher stirring speed. This confirms that an increase in stirring speed, regardless of solid content, leads to better suspension, allowing larger particles to enter the FGD.

The combined consideration of the impacts of stirring speed and solid content shows that the solid content has an even greater impact on the classification than the stirring speed. For a solid content of 1 wt%, the smallest values of $x_{50,Prod}$ and $x_{25,Prod}$ are observed. For the solid contents of 3 wt% and 5 wt%, the best classification with the highest values for $x_{50,Prod}$ and $x_{75,Prod}$ and therefore the highest product quality are achieved. In contrast to 3 wt%, the values at 5 wt% are not constant and increase for higher stirring speeds. These results can be explained by a balance between suspension and sedimentation that has to be found for the optimal operation of a DTBC. The stirring speed has a direct impact on the suspension state in the DTBC and thus, on the particle density in the sedimentation zone. However, a high energy input by the stirrer can also impairs classification performance. With an almost homogeneous suspension, the cut-off particle size can increase so much that too

many larger particles enter the FGD, where they can no longer be dissolved. Additionally, sedimentation into the product removal is minimized, which results in suspension is drawn into the product removal without classification and therefore in lower product quality. Therefore, the stirring speed must be adjusted according to the solid content.

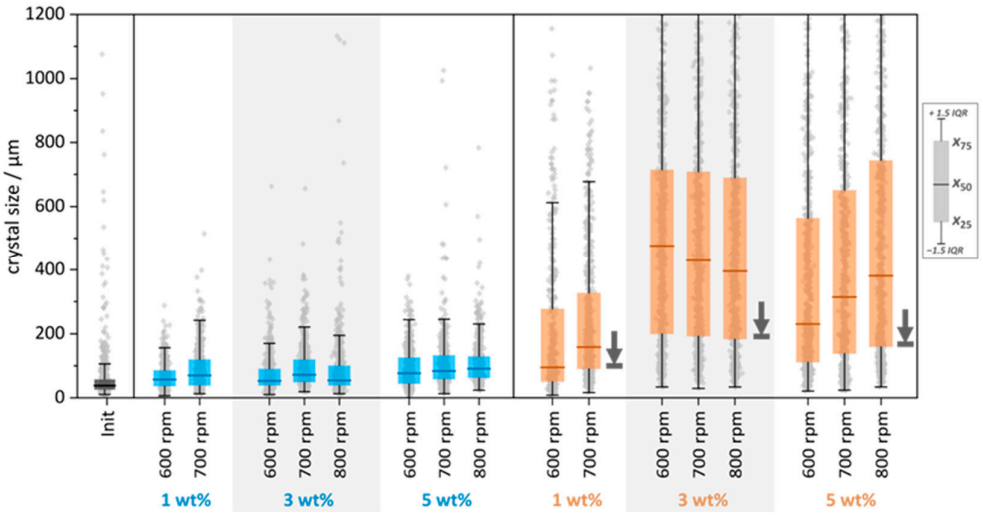


Figure 7. Boxplots comparing CSD_{FGD} (**blue**) and CSD_{Prod} (**orange**) for different solid fractions in suspensions and different stirring speeds at $\dot{V}_{FGD}$ = 30 mL min^{-1} and $\dot{V}_{Prod}$ = 20 mL min^{-1} with CSD_{init} (**grey**). Arrows indicate the change in $x_{25,Prod}$ height for different solid fractions.

For a solid content of 5 wt%, all three statistical values increase with rising stirring speed in the CSD_{Prod}. At 800 rpm, the maximum value of approximately $x_{75,Prod}$ = 750 µm, is reached. Consequently, for a solid content of 5 wt%, stirring speeds above 700 rpm are advantageous, as sufficient energy is introduced to increase the cut-off particle size for an optimized CSD_{Prod}. For a solid content of 1 wt%, the lowest product quality is observed at the considered stirring speeds. This can be attributed to an excessively high stirring speed, which results in an almost homogeneous suspension in the DTBC. For suspensions with a solids content of less than 3 wt%, a maximum stirring speed of 500 rpm should therefore be set to obtain a CSD_{Prod} with a high $x_{50,Prod}$. Since the suspension behavior for a suspension with a solids content of 3 wt% has not yet been investigated at 500 rpm, further investigations are necessary to confirm this assumption.

The highest values for $x_{50,Prod}$ and $x_{25,Prod}$, and thus the best classification performance, were obtained at a solid content of 3 wt%. Across all three stirring speeds, $x_{25,Prod}$ remained constant at approximately 200 µm. For $x_{50,Prod}$, a decreasing trend with increasing stirring speed was observed, the values are declining from about 500 µm to 450 µm at 700 rpm and to 400 µm at 800 rpm. The operating point with the highest $x_{50,Prod}$ value and the narrowest CSD_{Prod} is therefore observed at 3 wt%, 600 rpm, $\dot{V}_{Prod}$ = 20 mL min^{-1}, and a flow rate in the FGD of $\dot{V}_{FGD}$ = 30 mL min^{-1}.

4. Conclusions

In this study a newly developed gate system is presented for a continuous product removal for laboratory-scale vacuum crystallization. Over continuous testing periods lasting up to 6 h per experiment and cumulatively exceeding for 30 h, no blockages occurred in the product removal. This demonstrates the reliability of the system as a removal system for solid products and also illustrates a potential approach to overcoming challenges in product removal for other lab-scale vacuum applications.

Furthermore, this study investigated the optimization of the crystallization process in a 2.1 L draft tube baffle crystallizer (DTBC) through selective product removal by adjusting

process parameters. Systematic experiments were conducted to evaluate classification performance, with crystal size distributions (CSD) in the fine grain dissolution and product analyzed based on statistical values.

The results demonstrated a clear and expected effect of the flow rate in the fine grain dissolution on classification, as it directly influences the cut-off particle size. While previous studies on larger-scale DTBC systems have primarily linked flow rate effects to residence time, this work revealed that higher volume flow rates in the product removal directly impact classification within the DTBC. Specifically, higher product removal rates accelerate particle settling velocity, resulting in CSDs with larger particles in the product. In general, higher flow rates in the fine grain dissolution and higher product removal rates promoted improved classification outcomes for the CSD in the product.

The stirring speed also emerged as a critical parameter due to its influence on the suspension and the height of the sedimentation zone in the DTBC body. In order to achieve an optimal classification in the DTBC, a balance has to be maintained between suspension and sedimentation. The energy input from the stirrer needs to be sufficient to increase the cut-off particle size. However, the stirring speed should not be set too high to avoid an almost homogeneous suspension. This would minimize the sedimentation of larger particles in the product removal and thus reduce product quality. Therefore, the stirring speed must be adjusted according to solid fraction. For this DTBC setup, the optimal range was identified at 500–600 rpm for a solid fraction of 3 wt%, where the best operating point with the narrowest crystal size distribution in the product was achieved. Lower stirring speed of <400 rpm is recommended for lower solid fractions such as 1 wt%, while higher stirring speeds of >700 rpm are preferable for solid fractions of 5 wt%. Additional experiments are needed to validate these results across solid contents ranging from 3–7 wt% and stirring speeds between 400–800 rpm.

The results in this work establish a foundation for the operation of a lab-scale DTBC by enabling an assessment of how process parameter variations influence the CSD in the fine grain dissolution and the product. As the present study focused on the suspension behavior of crystals while neglecting crystal growth, additional investigations are required to translate these results to an actual crystallization process. In this context, it must be considered that, particularly during the start-up phase, the solid content increases dynamically until a balance between abrasion and nucleation is established in the DTBC.

For future work, additional analytical methods, such as X-ray diffraction, can be employed to study the crystallization process in more detail, particularly to monitor crystal form and size during nucleation and growth. Moreover, more complex interactions are expected when crystallization dynamics are included. In such cases, machine learning approaches, e.g., random forest models such as XGBoost, can be applied to evaluate multifactorial interdependencies. The results obtained here can thus serve as a basis for future studies and control strategies aimed at ensuring consistent product quality throughout the entire crystallization process.

Additionally, the shown operating ranges refer specifically to the used test system L-alanine in water. For substance systems with different density differences or crystal shapes, the trends discussed are generally transferable, as the effects described occur independently of these parameters. However, the specified operating ranges may differ, because for the suspension of particles with a higher density differences greater energy input from the stirrer is required. Therefore, repeating the experiments is necessary to define the operating ranges for other substance systems.

Supplementary Materials: The following supporting information can be downloaded at: https://www.mdpi.com/article/10.3390/cryst15100893/s1, Section S1: Key physical and chemical properties of used L-alanine; Table S1: Equipment and manufacturer information of all equipment

used in the experimental setup; Figure S1: Geometry of the used DTBC; Figure S2: Procedure of sample preparation according to Höving et al.; Figure S3: Analytic setup for Image Analysis; Section S2: Calibration Camera; Figure S4: Schematic representation of pneumatic pinch valves; Figure S5: Technical drawing of the gate volume; Figure S6: Calibration of the pinch valves used in the automated gate system; Figure S7: HiText program for the control of the automated gate system; Section S3: Automation gate system; Figure S8: Settling zones in DTBC at different stirring speeds.

Author Contributions: Conceptualization: L.M.; methodology: L.M. and M.H.; validation: L.M. and M.H.; formal analysis: L.M. and M.H.; investigation: L.M., M.H. and K.B.; resources: N.K.; data curation: L.M. and M.H.; writing—original draft preparation: L.M. and M.H.; writing—review and editing: L.M. and N.K.; visualization: L.M. and M.H.; supervision: L.M. and N.K.; project administration: N.K.; funding acquisition: N.K. All authors have read and agreed to the published version of the manuscript.

Funding: This research was funded by the Federal Ministry for Economic Affairs and Climate Action (BMWK) as part of the ENPRO REUNION project (grant number 03EN2100B).

Data Availability Statement: The original contributions presented in the study are included in the article/Supplementary Materials. Further inquiries can be directed to the corresponding author/s.

Acknowledgments: The authors thank Carsten Schrömges (TU Dortmund University, BCI Laboratory of Equipment Design) for his technical support and the German Federal Ministry for Economic Affairs and Climate Action (BMWK) for funding this research as part of the ENPRO REUNION project (grant number 03EN2100B).

Declaration of Generative AI and AI-Assisted Technologies in the Writing Process: During the preparation of this work, the author used ChatGPT-5 mini in order to correct grammar and language. After using this tool/service, the authors reviewed and edited the content as needed and take full responsibility for the content of the publication.

Conflicts of Interest: On behalf of all authors, the corresponding authors state that there is no conflict of interest.

Abbreviations

The following abbreviations are used in this manuscript.

CFD	Computational Fluid Dynamics
CSD	Crystal Size Distribution
DTBC	Draft Tube Baffle Crystallizer
IQR	Interquartile Range
LED	Light Emitting Diode
OP	Operating Point
rpm	Revolutions per minute
SI	Supporting Information

References

1. Brown, C.J.; McGlone, T.; Yerdelen, S.; Srirambhatla, V.; Mabbott, F.; Gurung, R.; Briuglia, M.L.; Ahmed, B.; Polyzois, H.; McGinty, J.; et al. Enabling precision manufacturing of active pharmaceutical ingredients: Workflow for seeded cooling continuous crystallisations. *Mol. Syst. Des. Eng.* **2018**, *3*, 518–549. [CrossRef]
2. Domokos, A.; Nagy, B.; Szilágyi, B.; Marosi, G.; Nagy, Z.K. Integrated Continuous Pharmaceutical Technologies—A Review. *Org. Process Res. Dev.* **2021**, *25*, 721–739. [CrossRef]
3. Jiang, M.; Braatz, R.D. Designs of continuous-flow pharmaceutical crystallizers: Developments and practice. *CrystEngComm* **2019**, *21*, 3534–3551. [CrossRef]
4. Ma, Y.; Wu, S.; Macaringue, E.G.J.; Zhang, T.; Gong, J.; Wang, J. Recent Progress in Continuous Crystallization of Pharmaceutical Products: Precise Preparation and Control. *Org. Process Res. Dev.* **2020**, *24*, 1785–1801. [CrossRef]
5. Orehek, J.; Teslić, D.; Likozar, B. Continuous Crystallization Processes in Pharmaceutical Manufacturing: A Review. *Org. Process Res. Dev.* **2021**, *25*, 16–42. [CrossRef]

6. Vaidya, S.N.; Agrawal, S.; Lambole, V.; Pimpale, A.; Telrandhe, U. Pharmaceutical manufacturing continuous crystallization procedures: A review. *Asian J. Pharm.* **2023**, *17*, 344–354.
7. Wood, B.; Girard, K.P.; Polster, C.S.; Croker, D.M. Progress to Date in the Design and Operation of Continuous Crystallization Processes for Pharmaceutical Applications. *Org. Process Res. Dev.* **2019**, *23*, 122–144. [CrossRef]
8. Sen, M.; Rogers, A.; Singh, R.; Chaudhury, A.; John, J.; Ierapetritou, M.G.; Ramachandran, R. Flowsheet optimization of an integrated continuous purification-processing pharmaceutical manufacturing operation. *Chem. Eng. Sci.* **2013**, *102*, 56–66. [CrossRef]
9. Chen, J.; Sarma, B.; Evans, J.M.B.; Myerson, A.S. Pharmaceutical Crystallization. *Cryst. Growth Des.* **2011**, *11*, 887–895. [CrossRef]
10. Plumb, K. Continuous Processing in the Pharmaceutical Industry. *Chem. Eng. Res. Des.* **2005**, *83*, 730–738. [CrossRef]
11. Schaber, S.D.; Gerogiorgis, D.I.; Ramachandran, R.; Evans, J.M.B.; Barton, P.I.; Trout, B.L. Economic Analysis of Integrated Continuous and Batch Pharmaceutical Manufacturing: A Case Study. *Ind. Eng. Chem. Res.* **2011**, *50*, 10083–10092. [CrossRef]
12. Alison, L.; Seckler, M.; Kramer, H.; van Rosmalen, G. *Industrial Crystallization: Fundamentals and Applications*; Cambridge University Press: Cambridge, UK, 2015.
13. Mersmann, A. (Ed.) *Crystallization Technology Handbook*, 2nd ed.; Dekker: New York, NY, USA, 2001.
14. Melches, C.; Plate, H.; Schürhoff, J.; Buchfink, R. The Steps from Batchwise to Continuous Crystallization for a Fine Chemical: A Case Study. *Crystals* **2020**, *10*, 542. [CrossRef]
15. Caldwell, H.B. Modern Concepts of Crystallization. *Ind. Eng. Chem.* **1961**, *53*, 115–118. [CrossRef]
16. Kramer, H.J.; Bermingham, S.K.; van Rosmalen, G.M. Design of industrial crystallisers for a given product quality. *J. Cryst. Growth* **1999**, *198–199*, 729–737. [CrossRef]
17. Kramer, H.J.M.; Lakerveld, R. Selection and Design of Industrial Crystallizers. In *Handbook of Industrial Crystallization*; Myerson, A.S., Erdemir, D., Lee, A.Y., Eds.; Cambridge University Press: Cambridge, UK, 2019; pp. 197–215.
18. Xu, K.; Wang, C.; Wang, X.; Qian, Y. Laboratory experiments on simultaneous removal of K and P from synthetic and real urine for nutrient recycle by crystallization of magnesium–potassium–phosphate–hexahydrate in a draft tube and baffle reactor. *Chemosphere* **2012**, *88*, 219–223. [CrossRef]
19. Schmalenberg, M.; Mensing, L.; Lindemann, S.; Krell, T.; Kockmann, N. Miniaturized draft tube baffle crystallizer for continuous cooling crystallization. *Chem. Eng. Res. Des.* **2022**, *178*, 232–250. [CrossRef]
20. Hofmann, G. *Kristallisation in der Industriellen Praxis*; John Wiley & Sons: Hoboken, NJ, USA, 2004.
21. Neumann, A.M. Characterizing Industrial Crystallizers of Different Scale and Type. Ph.D. Thesis, Delft University of Technology, Delft, The Netherlands, 2001.
22. Pant, H.J. Flow rate measurements in a draft tube baffle crystallizer using a radioactive flow follower technique. *Appl. Radiat. Isot.* **2000**, *53*, 999–1004. [CrossRef]
23. Pan, H.; Li, J.; Jin, Y.; Yang, B.; Li, X. Numerical Investigation of the Effect of Bottom Shape on the Flow Field and Particle Suspension in a DTB Crystallizer. *Int. J. Chem. Eng.* **2016**, 6862152. [CrossRef]
24. Wantha, W.; Flood, A.E. Numerical Simulation and Analysis of Flow in a DTB Crystallizer. *Chem. Eng. Commun.* **2008**, *195*, 1345–1370. [CrossRef]
25. Eek, R.A.; Dijkstra, S.; van Rosmalen, G.M. Dynamic modeling of suspension crystallizers, using experimental data. *AIChE J.* **1995**, *41*, 571–584. [CrossRef]
26. ten Cate, A.; Bermingham, S.K.; Derksen, J.J.; Kramer, H.M. Compartmental modeling of an 1100L DTB crystallizer based on Large Eddy flow simulation. In Proceedings of the 10th European Conference, Delft, The Netherlands, 2–5 July 2000; pp. 255–264.
27. Sutradhar, B.C.; Randolph, A.D. Design charts for the fines-dissolving crystallizer. *Ind. Eng. Chem. Res.* **1993**, *32*, 2781–2788. [CrossRef]
28. Sotowa, K.-I.; Hamamura, T.; Taniguchi, H.; Kano, M.; Hasebe, S.; Hashimoto, I. Influence of the incomplete dissolution of fines in the fines dissolver on the optimal operation of industrial continuous DTB crystallizers. *Powder Technol.* **2001**, *121*, 93–98. [CrossRef]
29. Juzaszek, P.; Larson, M.A. Influence of fines dissolving on crystal size distribution in an MSMPR crystallizer. *AIChE J.* **1977**, *23*, 460–468. [CrossRef]
30. Oh, D.-H.; Jeon, R.-Y.; Kim, J.-H.; Lee, C.-H.; Oh, M.; Kim, K.-J. Scale-Up of a Semi-Batch Draft Tube Baffled Crystallizer for Hexanitrohexaazaisowurtzitane Based on Experiments and Computational Fluid Dynamics Simulation. *Cryst. Growth Des.* **2019**, *19*, 658–671. [CrossRef]
31. Schmalenberg, M.; Nocon, A.-K.; Kockmann, N. Design and Hydrodynamic Characterization of a Draft Tube Baffle Tank for Lab-Scale. *Chem. Ing. Tech.* **2020**, *92*, 288–294. [CrossRef]
32. Schmalenberg, M.; Krell, T.; Mathias, C.; Kockmann, N. Continuous Miniaturized Draft Tube Baffle Crystallizer with Particle Screw for Supportive Suspension Discharge. *Ind. Eng. Chem. Res.* **2021**, *60*, 18094–18105. [CrossRef]

33. Marsollek, L.; Knappstein, P.L.; Duncker, P.; Lamprecht, J.; Westkämper, N.; Kockmann, N. Conceptual Approach for Lab-Scale Vacuum DTB Crystallizer with Online Monitoring and Flexible Process Functionalities for Rapid Process Adjustment. *Chem. Ing. Tech.* **2025**, 1–7. [CrossRef]
34. Mueansichai, T.; Flood, A.E.; Stelzer, T.; Ulrich, J. Rate of sodium chloride attrition fragment generation in a mixed-suspension crystallizer. *Z. Für Exp. Tech. Krist.* **2013**, *48*, 38–50. [CrossRef]
35. Bode, K.; Hooper, R.J.; Paterson, W.R.; Wilson, D.I.; Augustin, W.; Scholl, S. Reinigung von Molkeproteinablagerungen mit pulsierender Strömung. *Chem. Ing. Tech.* **2006**, *78*, 613–620. [CrossRef]
36. Lührmann, M.-C.; Timmermann, J.; Schembecker, G.; Wohlgemuth, K. Enhanced Product Quality Control through Separation of Crystallization Phenomena in a Four-Stage MSMPR Cascade. *Cryst. Growth Des.* **2018**, *18*, 7323–7334. [CrossRef]
37. Sha, Z.; Oinas, P.; Louhi-Kultanen, M.; Yang, G.; Palosaari, S. Application of CFD simulation to suspension crystallization—factors affecting size-dependent classification. *Powder Technol.* **2001**, *121*, 20–25. [CrossRef]
38. Sha, Z.; Palosaari, S. Size Dependent Classification Function in Imperfectly Mixed Suspension Continuous Crystallizer. In *Mixing and Crystallization*; Springer: Dordrecht, The Netherlands, 2000; pp. 133–149.
39. Hasebe, S.; Hamamura, T.; Nagata, H.; Sotowa, K.-I.; Hashimoto, I. The effects of imperfect mixing on the stabilizing control of continuous DTB crystallizers. *IFAC Proc. Vol.* **2001**, *34*, 293–298. [CrossRef]
40. Sha, Z.; Palosaari, S. Mixing and crystallization in suspensions. *Chem. Eng. Sci.* **2000**, *55*, 1797–1806. [CrossRef]
41. Rielly, C.D.; Marquis, A.J. A particle's eye view of crystallizer fluid mechanics. *Chem. Eng. Sci.* **2001**, *56*, 2475–2493. [CrossRef]
42. Acevedo, D.; Peña, R.; Yang, Y.; Barton, A.; Firth, P.; Nagy, Z.K. Evaluation of mixed suspension mixed product removal crystallization processes coupled with a continuous filtration system. *Chem. Eng. Process. Process Intensif.* **2016**, *108*, 212–219. [CrossRef]
43. Yan, Z.; Wang, J.; Liu, W.; Lu, J. Apparent molar volumes and viscosity B-coefficients of some α-amino acids in aqueous solutions from 278.15 to 308.15K. *Thermochim. Acta* **1999**, *334*, 17–27. [CrossRef]
44. Wohlgemuth, K.; Schembecker, G. Modeling induced nucleation processes during batch cooling crystallization: A sequential parameter determination procedure. *Comput. Chem. Eng.* **2013**, *52*, 216–229. [CrossRef]
45. Randolph, A.D.; Beer, G.L.; Keener, J.P. Stability of the class II classified product crystallizer with fines removal. *AIChE J.* **1973**, *19*, 1140–1149. [CrossRef]
46. Höving, S.; Oldach, B.; Kockmann, N. Cooling Crystallization with Complex Temperature Profiles on a Quasi-Continuous and Modular Plant. *Processes* **2022**, *10*, 1047. [CrossRef]
47. Marsollek, L.; Lamprecht, J.; Kockmann, N. Investigation of AI Algorithms for Photometric Online Analysis in a Draft Tube Baffle Crystallizer. *Crystals* **2024**, *14*, 1045. [CrossRef]
48. Dekking, F.M.; Kraaikamp, C.; Lopuhaä, H.P.; Meester, L.E. *A Modern Introduction to Probability and Statistics: Understanding Why and How*; Springer-Verlag London Limited: London, UK, 2005.
49. Stiess, M. *Mechanische Verfahrenstechnik—Partikeltechnologie 1*, 3rd ed.; Springer: Berlin, Germany, 2008.
50. Kraume, M. *Mischen und Rühren: Grundlagen und Moderne Verfahren*; Wiley-VCH: Weinheim, Germany, 2003.

Disclaimer/Publisher's Note: The statements, opinions and data contained in all publications are solely those of the individual author(s) and contributor(s) and not of MDPI and/or the editor(s). MDPI and/or the editor(s) disclaim responsibility for any injury to people or property resulting from any ideas, methods, instructions or products referred to in the content.